ORIGINAL ARTICLE

Heat treatment effects on tribocorrosion resistance of Inconel 718® alloy produced by conventional and laser powder bed fusion methods

Daniel Wieczorek[1] · Dariusz Ulbrich[1] · Arkadiusz Stachowiak[1] · Konrad Gruber[2] · Dariusz Bartkowski[3] · Aneta Bartkowska[4] · Andrzej Miklaszewski[4]

Abstract

The article presents a study of the tribocorrosion phenomenon and its effects on Inconel 718 alloy produced conventionally by extrusion and additively manufactured using the laser powder bed fusion method. In addition, the samples were subjected to a heat treatment process to change their properties. The research was carried out using the pin-on-disk method in 3.5% NaCl. Based on the study, it was found that the material made with additive technology is more resistant to tribocorrosion phenomenon, and the difference from conventionally made material is about 50%. The synergistic effect between friction and corrosion (ΔZ) occurred. However, heat treatment in the AA-2 variant ensures higher hardness and reduces purely mechanical wear (Z_M) and the synergy effect (ΔZ).

Keywords Tribocorrosion · Inconel 718 · Laser powder bed fusion · Heat treatment

1 Introduction

The 3D printing technology has revolutionized the manufacturing industry because it allows to produce complex 3D objects using various materials [1, 2]. Additive manufacturing (AM) technology for metal alloys is currently well established, with laser powder bed fusion (LPBF) being the most widely used and mature method [3]. However, several other AM methods offer unique advantages and applications, including electron beam melting (EBM) [3], binder jetting (BJ) [4], and directed energy deposition (DED) [5, 6]. Additive technology allows for manufacturing objects with excellent mechanical properties, such as aerospace components [7], automotive parts [8], and medical implants [9] from different materials (stainless steel, titanium, aluminum alloys, and nickel-based superalloys [10]).

Inconel 718 (IN718) is a commonly used nickel-based alloy that exhibits excellent mechanical properties, high-temperature resistance, and good corrosion resistance [11–13]. It finds extensive applications in various industries where strength, corrosion resistance, and reliability are desirable. Inconel 718 alloy is used in the aerospace industry (turbine blades, discs, combustion chamber) [14], gas turbines and power generation (i.e., nuclear reactors) [15], oil and gas industry (wellhead equipment and valves) [16], automotive industry (engines in racing cars, turbocharger) [17], and medical industry (implants, surgical instruments) [18]. Such high potential applications of the IN718 make it necessary to study its properties, especially under difficult operating conditions. One of the destructive effects on machine components is the phenomenon of tribocorrosion. An important factor necessary for the occurrence of tribocorrosion is the fact that the frictional cooperation of machine elements takes place in a corrosive environment. In many industries (food, oil, mining) the media used (processed products, raw materials) are electrolytes. The occurrence of tribocorrosion depends on many factors, such as the type of material, environmental

✉ Dariusz Bartkowski
dariusz.bartkowski@put.poznan.pl

1 Faculty of Civil and Transport Engineering, Poznan University of Technology, Marii Sklodowskiej-Curie 5 sq., Poznan 60-965, Poland

2 Faculty of Mechanical Engineering, Wroclaw University of Science and Technology, Lukasiewicza 5 street, Wroclaw 50-371, Poland

3 Faculty of Mechanical Engineering, Poznan University of Technology, Piotrowo 3 street, Poznan 61-138, Poland

4 Faculty of Materials Engineering and Technical Physics, Poznan University of Technology, Jana Pawla II 24, Poznan 61-138, Poland

conditions, the type and intensity of mechanical loads, and the presence of chemical substances.

Tribocorrosion is the simultaneous occurrence of both tribological phenomena (related to friction, wear, and lubrication) and corrosion in a material during its operation [19–21]. It is a complex interaction that arises when a material is exposed to both mechanical wear or frictional forces and corrosive environments. The combined effect of tribological and corrosive factors can lead to accelerated material degradation, which is often more severe than the sum of individual tribological or corrosion processes [22]. Tribocorrosion can result in increased wear rates, surface damage, material loss, changes in surface roughness, increased friction, and reduced mechanical performance [23–25].

The presence of a highly corrosive environment can significantly increase the loss of metal due to abrasive wear [26]. Studies on additively manufactured IN718 alloy indicate that from the point of view of corrosion resistance, manufacturing parameters, especially scan speed, are important [27]. Research shows [28–30] that the properties of nickel-based alloys, including hardness, phase precipitation kinetics, and corrosion resistance, can be modified through heat treatment. A recent study revealed that the corrosion resistance of IN718 can be greatly improved by solution annealing treatment at 1020 °C, which reduces corrosion microcracks [28].

Investigation of the tribocorrosion behavior of IN625 in seawater confirmed that the wear of this material was caused by a synergistic effect (which accounts for 86% of total material loss) between mechanical wear and corrosion [31]. Other studies have led to the conclusion that additive manufacturing technology has higher passivation capacity and lower susceptibility to cracking compared to wrought materials due to almost constant current density during the passive period for AM material [32]. A limited study of the tribocorrosion process additively manufactured IN718 [33] showed that the corrosive environment increases the wear of the test samples by less than 30%. The above test results do not explain the effect of heat treatments on friction resistance in corrosive environments for the additively manufactured IN718 material. Furthermore, no comparison of the results of the study of the tribocorrosion process of the IN718 material made by conventional methods and 3D printing technology was encountered.

The main objective of the research presented in the article was a comparative evaluation of the resistance to tribocorrosion in a 3.5% NaCl solution of IN718 material obtained by the conventional manufacturing process and the laser powder bed fusion method, taking into account the influence of two variants of heat treatment. In addition, research results allow for identifying the relationship between the intensity of the tribocorrosion and the structure as well as the properties of IN718 produced by different manufacturing

techniques and varied heat treatment parameters. The heat treatment parameters were selected based on the IN718 casting data sheet, which includes applicable heat treatment steps. An important novelty of the research presented in the article is the comparison of IN718, which was produced by different methods (conventional process and LPBF method) and subjected to different heat treatment processes in terms of resistance to tribocorrosion. As shown in the literature review, there is a lack of information on the phenomenon of tribocorrosion for IN718 material made with LPBF technology and after heat treatment. There is also a lack of knowledge regarding the comparison of tribocorrosion resistance for IN718 material produced by different methods. The following sections of the article detail the test methodology, including the preparation of the samples with heat treatment, the method used to evaluate tribocorrosion, and wear results (quantitative – volumetric wear and qualitative – SEM images of the surface after tribocorrosion wear). A detailed discussion of the results in relation to the literature is included, and the conclusion also presents directions for further research.

2 Research methodology

2.1 Samples

To produce laser powder bed fused samples, the argon-atomized Inconel 718 powder is supplied by SLM Solutions Group AG, Germany. The powder size distribution is confirmed using the HELOS H3776 and RODOS/T4/R4 laser diffraction system from Sympatec GmbH, Germany. The powder morphology is confirmed with the use of an EVO MA25 SEM microscope (Carl Zeiss AG, Germany). The chemical composition was checked using the X-ray fluorescence (XRF) spectrometer SPECTRO XEPOS from METEK, Germany. The nominal powder size distribution is 10–45 μm, while the measured distribution is $x_{10} = 22.63$ μm, $x_{50} = 34.88$ μm, and $x_{90} = 50.30$ μm. The powder particles are mainly spherical and spheroidal, with a small number of satellites. The chemical composition of the powder is within the standard limits of ASTM-F3055-14a and ASTM B637 (Table 1).

Rod Inconel 718 samples are delivered by Carpenter Technology Corporation in the form of a 1 m long, 12.7 mm dia. rod. Rod specification is according to the AMS 5662 standard. Rod samples are produced by an extrusion process and supplied in the annealed condition, i.e., held at 955 °C for 1 h and quenched in water. The chemical composition of the rod samples is also shown in Table 1.

LPBF samples are fabricated using the SLM 280 2.0 Dual PBF-LB/M machine from SLM Solutions Group AG. Reduced build volume is used together with a 98 mm × 98

mm × 15 mm Inconel 625 build plate. The building plate is heated to 200 °C, and the temperature is maintained throughout the process. Technical argon (class 4.6) is used as a process gas. To fabricate samples, a 700 W laser source with a 100 μm spot size is used. Previously tested and optimized process parameters are used: 300 W laser power, 1300 mm/s scanning speed, 120 μm hatch distance, and 30 μm layer thickness. The chosen scanning strategy is "Stripes," which divides the scanned cross-section into 7 mm wide sections, scanned subsequently. Each layer, the scanning vectors' direction, and the division of the cross section into stripes are rotated by 67°.

Both the LPBF and rod samples are cut into 40 mm bars prior to heat treatment (step 2 in Fig. 1) and into 5-mm discs after heat treatment (step 3 in Fig. 1) to prepare samples for the tribocorrosion test. The schematic

representation of the sample preparation is shown in Fig. 1.

Both laser powder bed fused and Rod Inconel 718 samples are subjected to post-process heat treatment (HT) which parameters were selected based on the IN718 casting data sheet that includes applicable heat treatment steps. Samples are divided into 4 groups: LPBF-1, LPBF-2, ROD-1, and ROD-2. Therefore, there are two different heat treatment routes for two materials. To heat treat the samples, the TAV H3S 1600 high-temperature vacuum furnace from TAV Vacuum Furnaces SPA, Italy, is used. Samples are processed under an atmosphere of technical argon (class 4.6). The heat treatment variants used for all sample groups are summarized in Table 2 and Fig. 2.

LPBF-1 and LPBF-2 samples are stress relieved (SR) while remaining on the build plate. After the process, the

Table 1 Chemical composition of Inconel 718 powder and rod used in the study [% wt.]

Type	Ni	Cr	Fe	Mo	Nb	Ti	Al	Ta	Co	C	Mn	Si	P
Powder	55.30	16.30	18.35	3.03	5.05	0.85	0.52	0.37	0.08	0.04	0.02	0.04	0.05
Rod	53.20	18.40	17.8	2.91	5.26	0.90	0.54	0.01	0.42	0.03	0.07	0.07	0.01

Fig. 1 Schematic representation of sample preparation and sample series used in the study: 1a, 1b, 2, 3—production steps for samples manufactured by LPBF and conventional methods
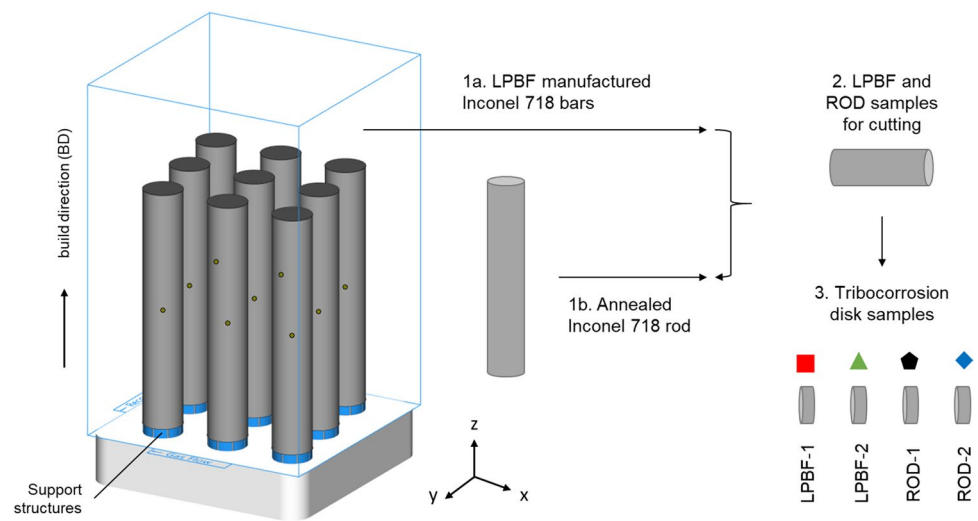

Table 2 Heat treatment variants for the LPBF-ed and Rod Inconel 718 sample series used in the study

Type	LPBF-1	LPBF-2	ROD-1	ROD-2
Material	LPBF-ed IN718	LPBF-ed IN718	Rod Inconel 718	Rod Inconel 718
SR	1065 °C/1 h/FC	1065 °C/1 h/FC	955 °C/1 h/WQ*	955 °C/1 h/WQ*
Simulated HIP	1150 °C/4 h/FC	1150 °C/4 h/FC	1150 °C/4 h/FC	1150 °C/4 h/FC
SA	1100 °C/1 h/AQ	1100 °C/1 h /AQ	1100 °C/1 h/AQ	1100 °C/1 h/AQ
AA-1	720 °C/8 h/FC to 620 °C/10 h/AC	-	720 °C/8 h/FC to 620 °C/10 h/AC	-
AA-2	-	760 °C/8 h /AC	-	760 °C/8 h/AC

*as delivered by Carpenter Technology Corp

SR stress relief annealing (LPBF)/annealing (ROD), *Simulated HIP* time and temperature used to hot isostatically press Inconel 718 according to ASTM F3055-14a standard, *SA* solution annealing, *AA* artificial aging, *FC* furnace cooling, *WQ* water quenching, *AQ* argon quenching, *AC* argon cooling

Fig. 2 Scheme of heat treatment process considering solution annealing (SA) step after simulated HIP and the type of artificial aging (AA); cooling types according to Table 2: **a** AA-1, **b** AA-2
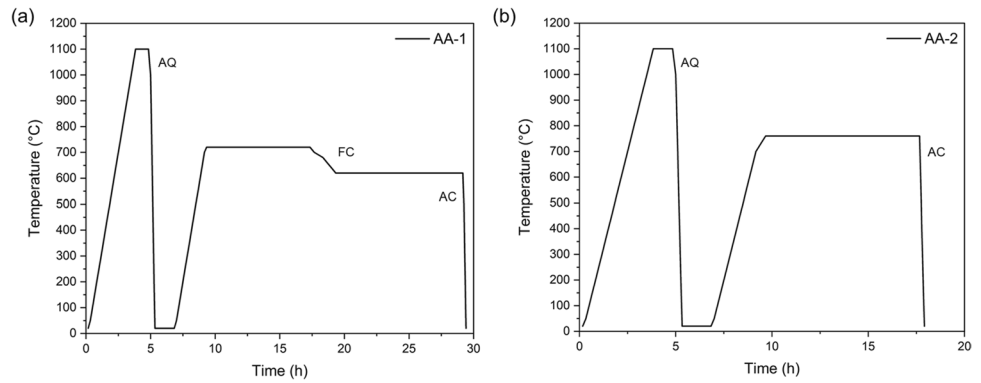
samples were cooled down with a furnace (FC), still under an argon atmosphere. The rod samples were delivered annealed. Therefore, SR is not performed for the rod samples. The second step of HT is simulated HIP, performed to mimic the time and temperature used for hot isostatic pressing (HIP) of critical Inconel 718 parts as per the ASTM-F3055-14a standard. After simulated HIP, the samples are also cooled in the furnace. The third HT step is solution annealing, after the SA process, the samples are cooled in the furnace at 10 bar abs with fan-assisted argon circulation (AQ–argon quenching). After the same HIP and SA, two different artificial aging routes are utilized. Route number 1 (AA-1) is used to heat-treat LPBF-1 and ROD-1 samples, and route number 2 (AA-2) is used to heat-treat LPBF-2 and ROD-2 samples. Rod samples undergo the same simulated HIP-SA-AA processes to maintain comparability against laser powder bed fused material.

2.2 Research methodology

The microstructure of the samples was examined using a MIRA-3 scanning electron microscope from TESCAN (Brno, Czech Republic). Cross sections of the specimens were observed using both secondary electrons (SE) and backscattered electrons (BSE) at various levels of magnification. Before the observation, all samples were ground with sandpapers of different grit sizes ranging from 80 to 2000. Then, the polishing in a diamond suspension was used in order to reduce polishing time. Finally, for polishing, the

deagglomerated gamma-alumina powder 0.05 μm in diameter was used. In the last step, the specimens were subjected to a 20-s etching process using Kalling's solution. The chemical composition of the specimens was analyzed using energy dispersive spectroscopy (EDS). For this purpose, an Ultim Max energy dispersive spectrometer from Oxford Instruments in High Wycombe, UK, was used. The Aztec Energy Live Standard software was used to analyze the measurements of element content. Point analysis was used to determine the composition of the elements, while EDS mapping was used to investigate chemical separation.

Microhardness tests were conducted on the cross-sections of the samples. Measurements were performed for each material, and the results, along with the arithmetic average, are presented in the subsequent section of the article. The FM-810 microhardness tester from Future-Tech in Kawasaki, Japan, was used for this study. The tester was equipped with FT-Zero software for automatic indentation measurement. The microhardness tests were carried out with an indentation load of 50 g, and the loading time for each test was 15 s.

The study of the tribocorrosion process was carried out using a ball-on-plate model node and a dedicated stand presented in papers [34, 35]. The test stand for tribocorrosion research is shown in Fig. 3. The study used disc-shaped samples with a diameter of 16 mm (additively manufactured material) and 12 mm (material produced by conventional technology) and a thickness of 8 mm. The samples prepared in this way were placed in a special holder inside a chamber with a corrosive

Fig. 3 Test stand for tribocorrosion research: **a** scheme, **b** view of the test chamber; 1 – linear guideway, 2 – applied weight, 3 – drive, 4 – reference electrode, 5 – counter electrode (wound platinum wire), 6 – ball, 7 – specimen (working electrode), 8 – PVC cell, 9 – stand (table)
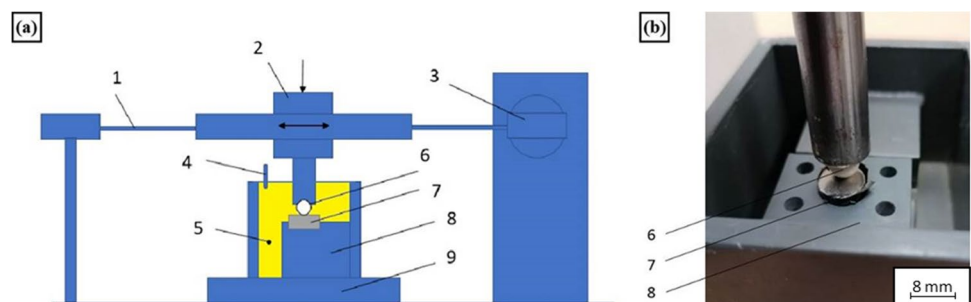
environment. The model environment was 3.5% NaCl (approximately 60 ml). A 7.0 mm diameter aluminum oxide ball was used as a counter-sample. The tests involving wear testing lasted about 40 min and consisted of 7200 displacements of the ball along the surface of the sample. The ball slid at an average speed of about 18 mm/s in a reciprocating motion over a distance of 6 mm. The tests were carried out with a ball loading force of approximately 10N, which guarantees an initial contact zone pressure of 1600 MPa.

The volumetric loss of material was determined based on profilometric measurements of the wear trace. These measurements were taken at the halfway point of friction after the tests were completed. The volumetric wear of the sample served as an indicator of its wear resistance.

To monitor the electrochemical parameters at the tested joint, an ATLAS 9833 potentiostat with three electrodes was used. The electrochemical parameters included the open-circuit potential (OCP) and the determination of polarization curves. The reference electrode used was a calomel electrode (SCE), while the auxiliary electrode was a platinum grid. To prevent any interference, the sample area outside the wear mark was shielded with a non-conductive strip.

The study of IN718 was designed to identify the combined effect of friction and corrosion (ΔZ) on the overall material loss during tribocorrosion (Z_T). According to the general concept, tribocorrosion wear consists of three components:

$$Z_T = Z_M + Z_K + \triangle Z \qquad (1)$$

where Z_M represents the loss of material solely caused by mechanical actions, and Z_K represents the loss of material solely caused by corrosive influences.

The corrosion-only component (Z_K) is a result of electrochemical processes occurring on the sample's surface when immersed in the electrolyte under static conditions, without frictional interactions. The value of the Z_K component was determined using Faraday's equation, taking into account the corrosion current density and the test duration. The purely mechanical component (Z_M) was determined through an independent experiment. The sample wear was tested in a 3.5% NaCl environment, but under cathodic polarization conditions to eliminate electrochemical processes on the sample surface while maintaining the lubricating properties of the environment. The difference ($\Delta Z = Z_T - Z_M - Z_K$) was ultimately used to quantify the interaction between friction and corrosion.

Following the tribocorrosion tests, an analysis of the surface condition was conducted. The authors of the study focused on determining the wear mechanism and the amount of wear of the tested materials.

3 Results of research

3.1 Microstructure and microhardness

Figure 4 shows the microstructure of the Inconel 718 specimen both in the form of a rod as well as an additively manufactured sample, all after heat treatment processes for variants AA-1 and AA-2. The microstructure of Inconel 718 alloy in the form of rod (ROD-1 and ROD-2) is characterized by a larger grain size than the microstructure obtained during the additive manufacturing process (LPBF-1 and LPBF-2). Due to the high temperature of the SR, HIP, and SA steps, the LPBF-1 and LPBF-2 samples lack the typical LPBF microstructure, described in detail in our previous study [36], exhibiting equiaxed γ grains, accompanied by twin boundaries. The grain size of Inconel 718 in the form of rod also shown in our previous study was comparable to its additively manufactured counterpart. Nevertheless, due to the same heat treatment, it suffered a significant grain size growth. As studies show [37–39], the LPBF-fabricated Inconel 718 manufactured by LPBF is resistant to grain growth at high temperatures and soaking times up to 1180 °C and 12 h. The size of the precipitates observed in the area of grains is influenced by the applied type of heat treatment. The artificial aging processes for Inconel 718 in the form of a rod were compared. It can be seen that as a result of the AA-1 operation (aging at 720 °C/8 h and then at 620 °C/10 h), grains with more niobium and titanium carbide precipitates were obtained (Fig. 4a). For specimens made in additive manufacturing technology, a similar dependence artificial aging influence on microstructure was observed (Fig. 4c). To identify the types of precipitates, a chemical composition study was carried out using qualitative (Fig. 5) and quantitative (Fig. 6, Table 3) EDS analysis. Figure 5 presents images of microstructures in contrast to secondary electrons (SE) with additional EDS mapping of element distribution in the analyzed area. Nickel (as the main Inconel alloy component), carbon, titanium, molybdenum, and niobium (components of carbide precipitates) were considered. Based on the qualitative analysis, it was found that the precipitate was probably niobium and titanium carbides. Carbides are expected because it is recognized that initial microsegregation in LPBF-processed Inconel 718 results in the formation of (Nb, Ti)C carbides during the early stages of high-temperature homogenization [39]. These carbides are beneficial because they inhibit grain growth via the Zener pinning effect. Moreover, it is important to note that the microstructural examination of the additively produced samples did not reveal common LPBF defects such as lack of fusion (LOF) porosity. The selection of sample cross-sections for microstructural studies

Fig. 4 Microstructure of tested material; SE image: **a** ROD-1, **b** ROD-2, **c** LPBF-1, **d** LPBF-2
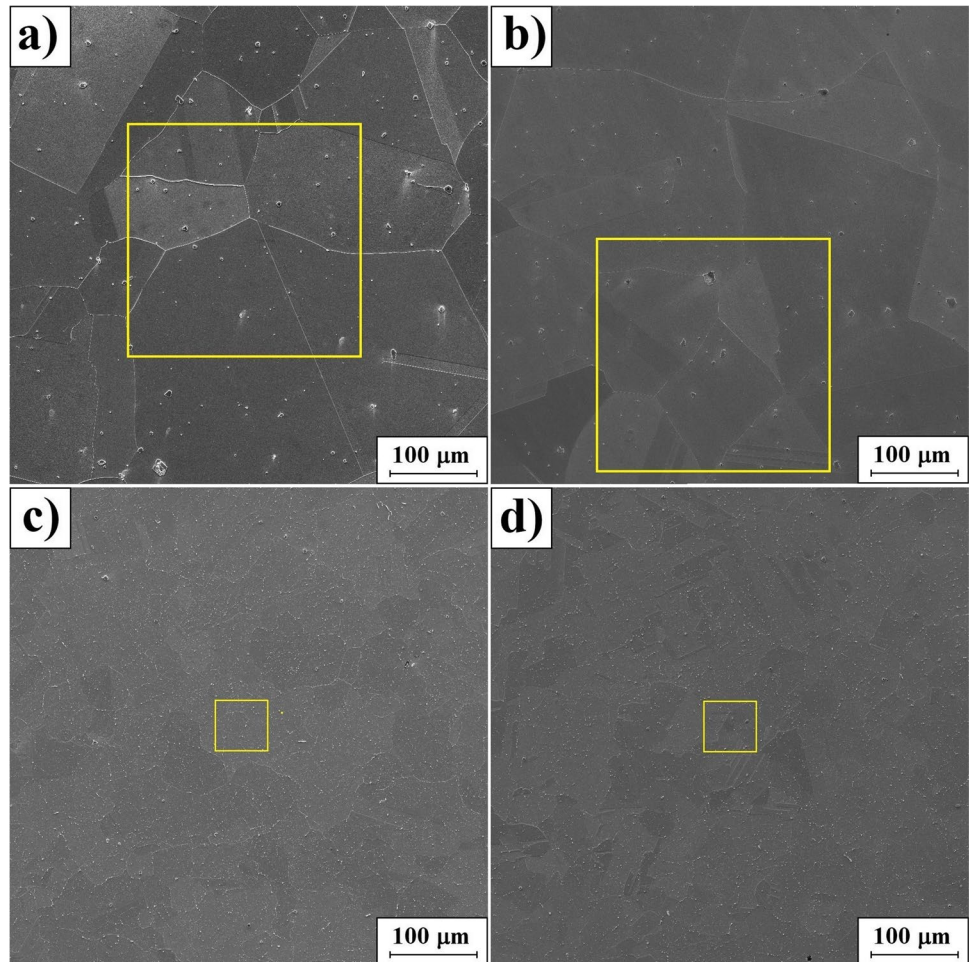
and tribocorrosion tests was deliberate to avoid subsurface defects. The LPBF process parameters and machine setup used in this study were identical to those used in reference [39], where Inconel 718 samples produced by LPBF exhibited LOF porosity primarily at the subsurface as shown by computed tomography reconstructions. In addition, our approach is consistent with the intended simulated HIP conditions designed for post-LPBF densification, which are intended to be replicated by our heat treatment route (see Table 2).

Due to very fine carbide precipitates (observed mainly in the grain and on the grain boundaries), spot tests of the chemical composition were carried out using the EDS method (Fig. 6, Table 3). Characteristic places of the microstructure were analyzed and marked by number: 1—larger precipitates, 2—smaller precipitates, and 3—matrix. The results obtained are presented in Table 3. Nitrogen, which favors the formation of carbonitrides, was also included in the EDS point analysis. In carbonitrides, part of the carbon content is replaced by nitrogen. Carbides and carbonitrides are formed by the strong tendency of C, N, and elements such as Ti and Nb to segregate during solidification. The

larger precipitates were enriched in niobium, whereas the smaller ones within the grains exhibited higher concentrations of titanium and nitrogen. This observation corresponds with findings from Inconel 625 welds [42], where intergranular, small NbC-type precipitates were found to be carbonitrides with cores rich in Ti and N, maintaining a consistent crystallographic structure despite compositional differences. The presence of nitrogen and titanium facilitates their nucleation during solidification, with niobium diffusion contributing to precipitate growth during subsequent heat treatment. This was particularly evident for Inconel 718 delivered in the form of a rod, where the precipitates had larger dimensions. The measurement of precipitations obtained during artificial aging for specimens made in additive manufacturing technology was somewhat difficult due to their very small dimensions. Hence, the presented results are a certain average value from the carbide present there and the substrate of the Inconel 718 alloy. The measurements made at point 3 corresponded to the chemical composition of the Inconel 718 alloy. Additionally, EDS mapping of niobium from the area marked in Fig. 4 was compiled to confirm the presented relationships in Fig. 7.

Fig. 5 Microstructure of tested material; SE/EDS image: **a** ROD-1, **b** ROD-2, **c** LPBF-1, **d** LPBF-2
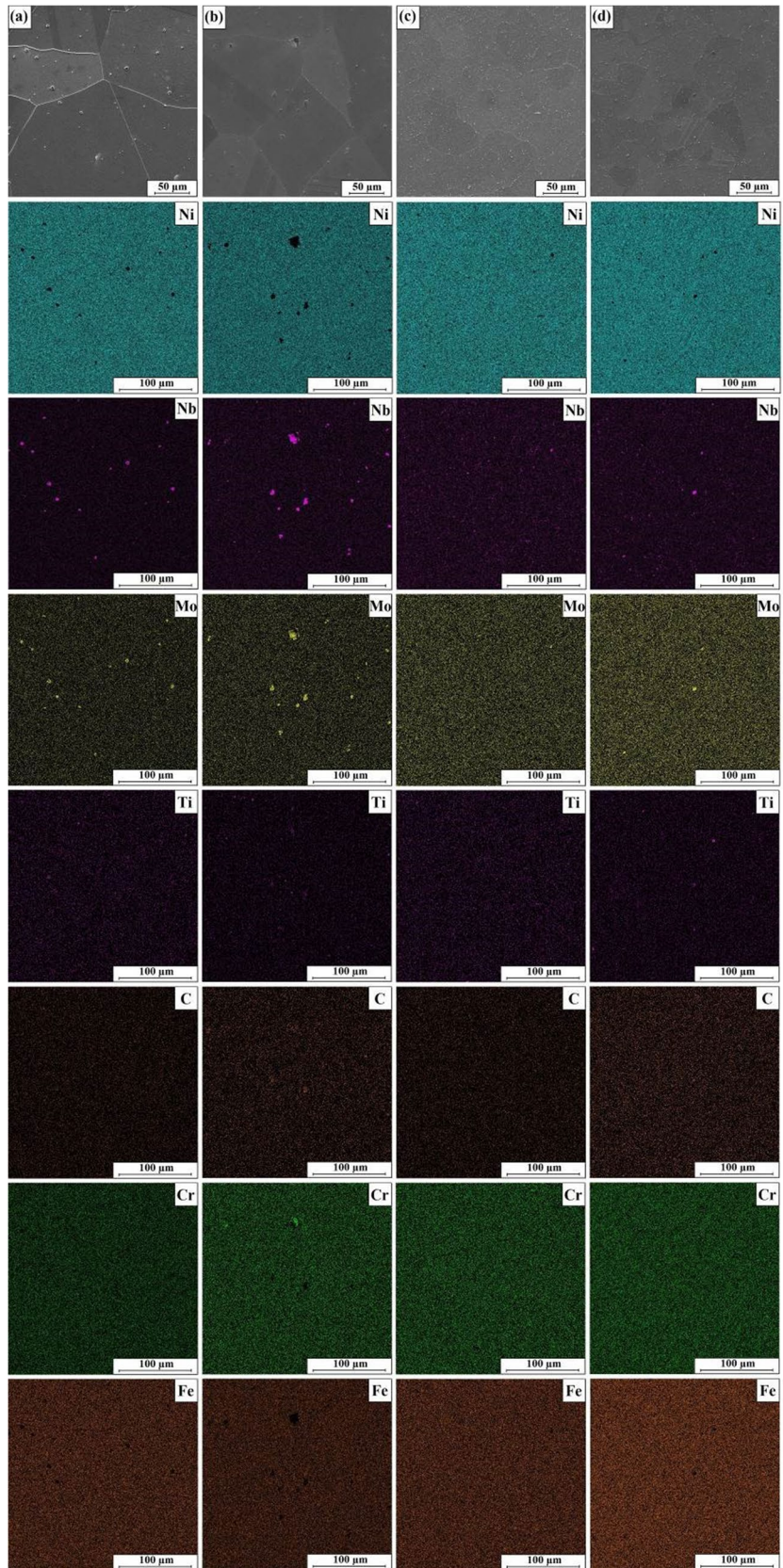
Fig. 6 Microstructure with marked area of measured chemical composition of EDS method: **a** ROD-1, **b** ROD-2, **c** LPBF-1, **d** LPBF-2
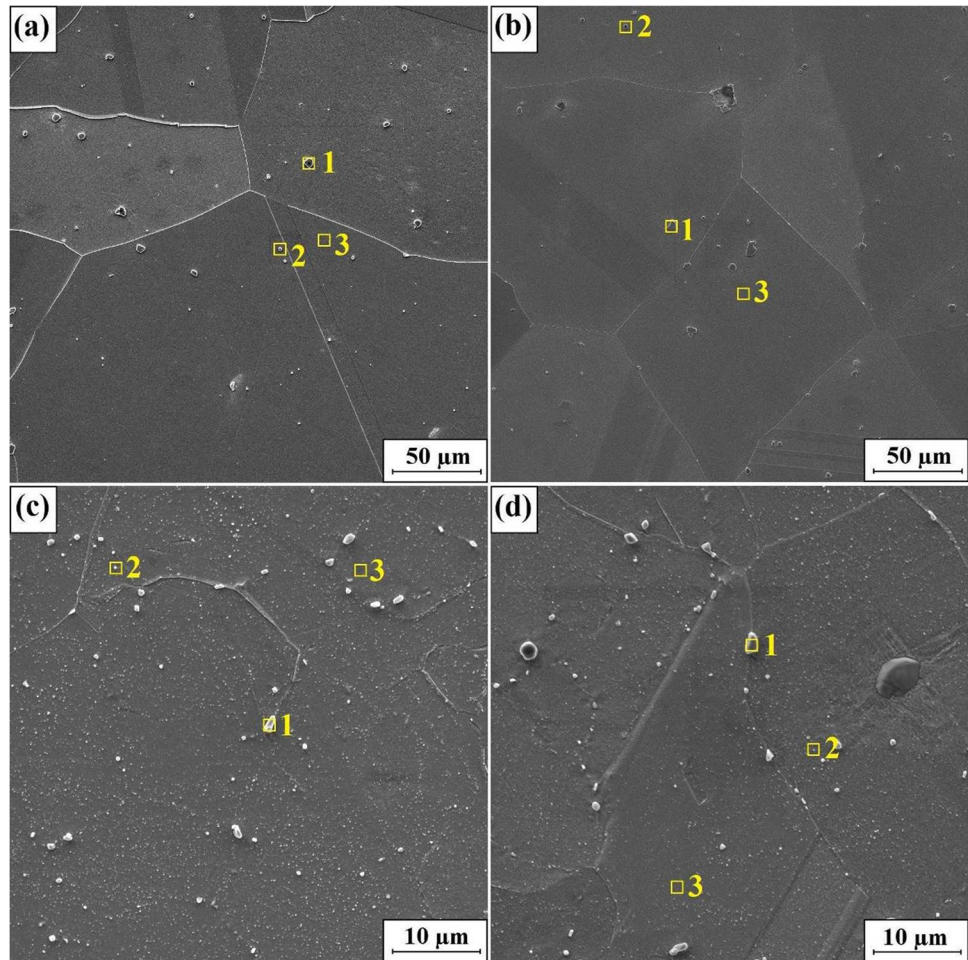

Table 3 Chemical composition by the EDS method for the areas marked in Fig. 6 [wt.%]

Designation	No	Ni	Fe	Cr	Nb	Mo	Ti	C	N
ROD-1	1	2.1	1.1	0.7	73.2	0.4	7.7	14.2	0.6
	2	15.5	6.2	7.8	7.9	1.4	44.1	3.9	13.3
	3	55.1	16.8	16.5	4.4	2.7	0.9	3.4	0.3
ROD-2	1	0.1	0.8	0.5	73.3	0.1	7.2	14.0	4.0
	2	23.5	7.6	7.6	17.5	1.4	29.7	2.6	10.2
	3	54.5	16.8	17.2	4.7	2.6	0.8	3.3	0.2
LPBF-1	1	1.7	0.9	0.9	65.5	0.0	9.3	20.5	1.3
	2	43.6	14.2	13.6	16.8	2.0	2.1	7.1	0.5
	3	52.0	17.5	17.4	4.5	3.0	0.8	4.4	0.4
LPBF-2	1	1.4	1.8	0.6	71.9	0.0	9.4	14.3	0.6
	2	14.6	5.7	6.0	52.6	1.4	6.8	12.2	0.8
	3	46.0	15.5	15.6	7.8	2.9	5.0	5.2	1.9

No other precipitates common to Inconel 718, such as Laves or δ phases, were found. The LPBF process parameters and machine setup used in this study (linear energy density below 0.30 J/mm and volumetric below 100 J/mm³) are identical to those used in references [39, 43]. This results in Laves phase particles in the as-built condition that are smaller and less numerous than in other studies [43]. The purpose of high-temperature solution annealing is to prevent the precipitation of undesirable phases, namely Laves and δ phases. After SA at 1100 °C/1 h, the microstructure showed no evidence of solute microsegregation, δ, or Laves phases, although it showed inhomogeneity due to grain boundary

Fig. 7 EDS mapping of niobium from the area marked in Fig. 4 and additionally presented in Fig. 6: **a** ROD-1, **b** ROD-2, **c** LPBF-1, **d** LPBF-2
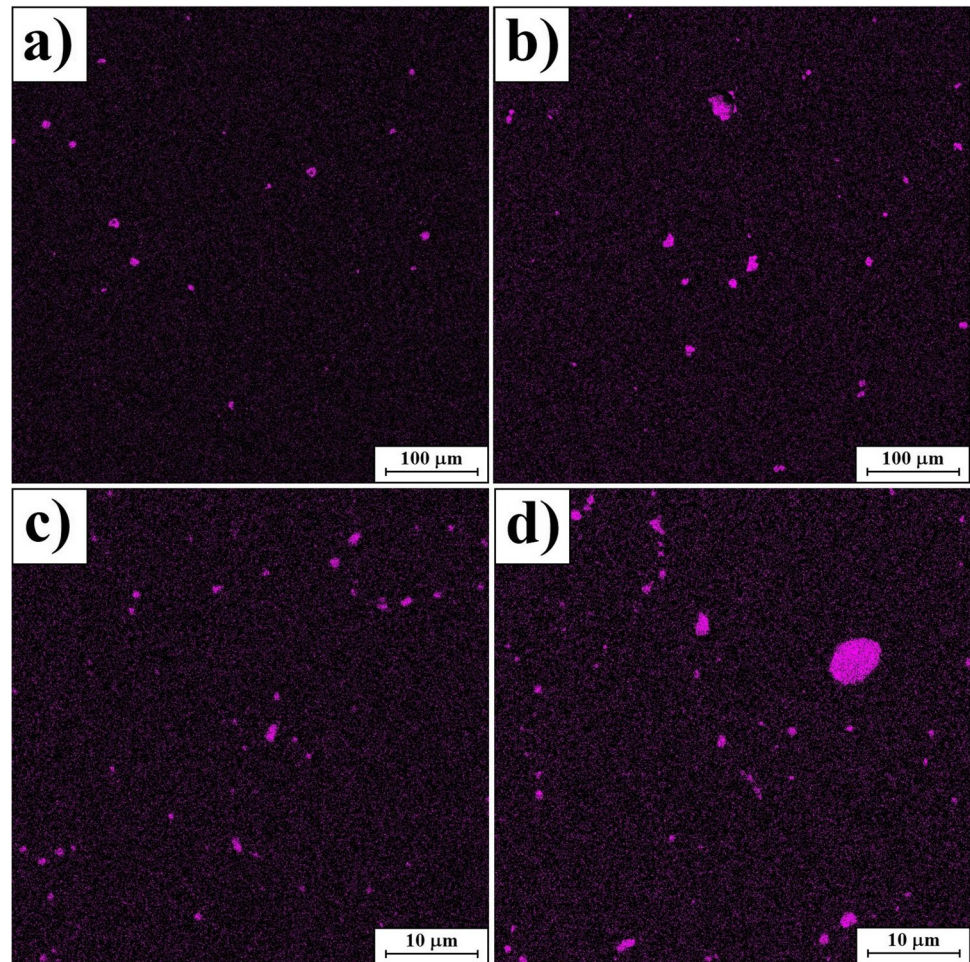

Table 4 Average microhardness values for all samples

HV$_{0.05}$	ROD-1	ROD-2	LPBF-1	LPBF-2
Value	539	501	508	545

diffusion of Nb, which also resulted in carbide coarsening. The cooling rate after SA of 140 °C/min, similar to the reference [39], was chosen to inhibit the precipitation of these phases in the homogenized alloy, as supported by previous results.

Table 4 presents the microhardness results for the analyzed samples. Based on the results, it should be stated that the samples after heat treatment were characterized by different average microhardness values. The highest hardness was characterized by a sample made by additive manufacturing according to the AA-2 heat treatment variant. Contrary, the lowest average hardness was obtained for the bar (ROD-2) subjected to heat treatment according to the AA-2 variant. The best properties of Inconel in the form of a rod were obtained as a result of heat treatment consisting of double aging (variant AA-1). As a result, an increased number of fine carbide precipitates was obtained. In the case of aging according to the AA-2 variant, no large amount of precipitates was observed in the microstructure, which could have contributed to lower microhardness. In the case of samples made using the additive method, the use of one- or two-stage aging resulted in the formation of numerous small precipitates. However, in the microstructure of the alloy aged according to the AA-2 variant, there were additionally larger NbC carbide precipitates, which could have an impact on the final microhardness. The aim of the research was to trace the changes occurring with two aging possibilities and two methods of obtaining the Inconel alloy (conventional method and printing method). Based on the presented research, it can be concluded that in the case of an additively manufactured alloy, it will be beneficial to use a one-stage aging process, also for economic and energy-intensive reasons. The increase in the microhardness of the alloy is confirmed by the EDS mapping results for niobium presented in Fig. 7, where larger NbC precipitations are visible.
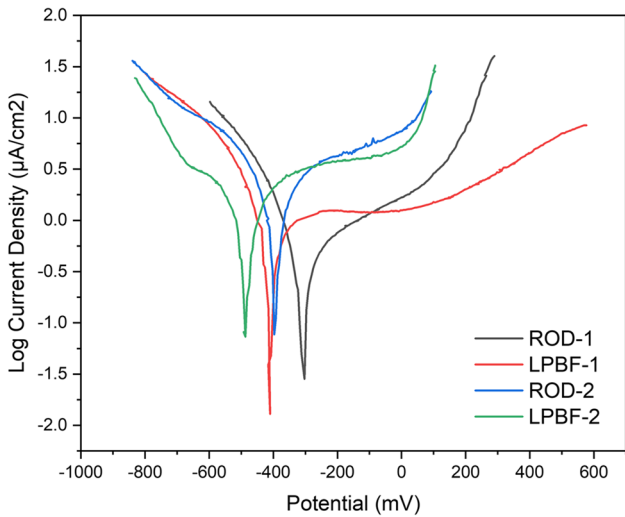
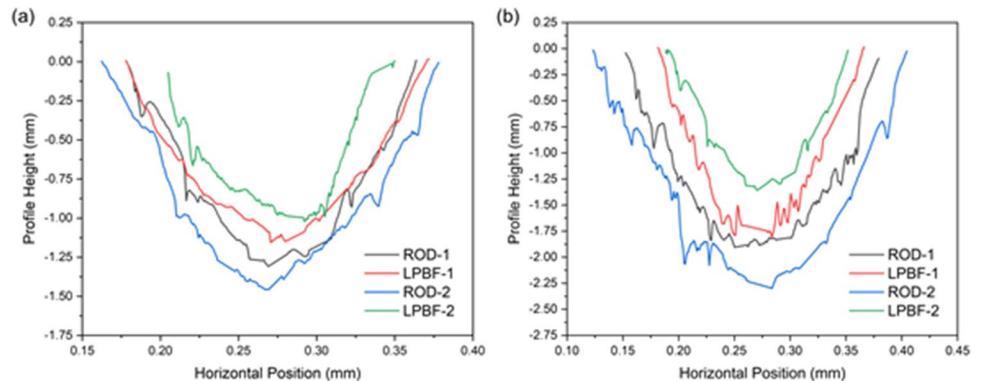**Fig. 8** Polarization curves of the tested materials (3.5% NaCl, 5 mV/s)

Table 5 Corrosion potential (E_{corr}) and corrosion current density (i_{corr})

Parameters	ROD-1	LPBF-1	ROD-2	LPBF-2
E_{corr}, mV (SCE)	-294 ± 12	-406 ± 15	-380 ± 14	-495 ± 16
$i_{corr,}$ μA/cm^2	0.93 ± 0.09	1.44 ± 0.15	2.82 ± 0.25	4.65 ± 0.28

3.2 Tribocorrosion test results

3.2.1 Potentiodynamic polarization curves and wear volume

Figure 8 presents the polarization curves of the tested materials in 3.5% NaCl. On the basis of these characteristics, using the Tafel method and AtlasLab software, the corrosion potential (E_{corr}) and corrosion current density (i_{corr}) were determined. The obtained results are shown in Table 5. Higher values of the corrosion current density indicate slightly worse resistance of the additively manufactured material to corrosion in 3.5% NaCl under static conditions (without friction). The relationship applies to both heat treatment variants.

The wear resistance test results are presented in Table 6. Primary tests were carried out under tribocorrosion conditions, specifically at the natural corrosion potential. Additional tests were performed with cathodic potential polarization, approximately −900 mV (SCE). The wear observed in the samples under these conditions corresponds to the mechanical component (Z_M) of the tribocorrosion wear. The volume of the wear trace served as a measure of the material's ability to withstand the destructive process. Table 6 also provides an assessment of the synergistic effect of friction and corrosion (ΔZ) and its contribution to the overall tribocorrosion wear. In Fig. 9, examples of wear trace profiles for tested materials are

Table 6 Experimental research results

Material/ type of aging	Material loss in the tribocorrosion (Z_T)	Mechanical component (Z_M)	Corrosion component (Z_K)	Synergistic effect (ΔZ)	$\Delta Z/Z_T$
	[mm^3] $\cdot 10^{-3}$	[mm^3] 10^{-3}	[mm^3] 10^{-3}	[mm^3] 10^{-3}	[%]
ROD-1	1.68 ± 0.12	0.78 ± 0.10	0.0011	0.89	53
LPBF-1	1.57 ± 0.11	0.92 ± 0.10	0.0017	0.65	41
ROD-2	2.04 ± 0.16	1.19 ± 0.13	0.0037	0.84	41
LPBF-2	1.27 ± 0.10	0.74 ± 0.10	0.0051	0.53	42

Fig. 9 Wear profiles of the tested materials after tests: **a** only mechanical wear, **b** tribocorrosion

displayed, showcasing the effects of tribocorrosion and only mechanical conditions.

The tribocorrosion wear (Z_T) of the IN718 material produced by the conventional process is 0.00168 mm^3 for the ROD-1 heat treatment variant and 0.00204 mm^3 for the ROD-2 heat treatment variant. In the case of specimens made by the laser powder bed fusion method, smaller material losses were found. The wear was equal to 0.00157 mm^3 for the LPBF-1 heat treatment variant and 0.00127 mm^3 for the LPBF-2 heat treatment variant, respectively.

Pure mechanical wear (Z_M) of the tested materials was in the range of 0.00074–0.00119 mm^3. The lowest value was found for the IN718 variant marked LPBF-2. On the other hand, the highest value was estimated for IN718 produced by the conventional technique and marked ROD-2 (and the corresponding heat treatment variant). For all analyzed variants of IN718 material, a clear synergistic effect of friction and corrosion was found (ΔZ). According to the data in Table 6, it ranged from 41 to 50%.

During the study of the tribocorrosion process, the value of the potential in the system was monitored. Changes in potential observed during tribocorrosion tests are characteristic of materials that exhibit passivation. When frictional interactions are initiated in the contact area between the sample and the counter-sample, a layer of passive oxides is removed from the material surface. This results in a decrease in potential. As soon as frictional excitations cease, the potential increases again due to the effective restoration of the passive layer over the entire surface of the wear trace.

3.2.2 Surface condition and chemical composition analysis after tribocorrosion tests

Figure 10 shows a scheme for selecting the site for the analysis of the surface condition after wear tests. The spot of a visible wear trace in the central part of the sample was marked by number 1. The area for detailed analysis of the surface after wear was marked by a yellow square marked 2. The area for qualitative chemical composition analysis using the EDS method was marked by a yellow square marked 3.

Figures 11, 12, 13, and 14 show the surface condition of the samples after wear tests and EDS mapping of the individual element distribution. Figure 10 shows a comparison of the sample surfaces after mechanical wear for AA-1 aging (stage 1: 720 °C/8 h, stage 2: 620 °C/10 h) of Inconel 718 alloy produced by conventional technique (Fig. 11a) and additive manufacturing technology (Fig. 11b). For both specimens, characteristic grooves can be seen on the wear surface. For the LPBF-1 sample, smaller changes caused by the counter-sample can be observed. It can be assumed that fine particles evenly distributed in the microstructure contributed to this. In Fig. 11, the wear surface is shown in two types of electron contrast (SE and BSE) and with the EDS mapping. Significant elements included in the Inconel 718 alloy such as Ni, Cr, Fe, C, and Nb were analyzed. They form tribocorrosion-reinforcing precipitates in the alloy in the form of niobium carbides, as well as oxygen-forming oxides which are associated with surface oxidation of the samples. On the wear surface, especially for LPBF samples, a large amount of fine niobium carbides is visible, which, due to their presence, inhibits the intensity of material wear.

Figure 12 shows a comparison of the surfaces of samples after one-stage aging marked as AA-2 and after mechanical wear for the Inconel 718 alloy produced by the conventional method (Fig. 12a) and by additive manufacturing technology (Fig. 12b). On the surface of the ROD-2 sample, there are clear traces of surface wear in the form of grooves (fissures) and chipping/tearing out caused by the work of the rubbing pair. In the case of the LPBF-2 specimen, the changes caused by friction were less intense.

Figures 13 and 14 show the wear surface of specimens after tribocorrosion tests. Figure 13 shows a comparison of the surface of the specimens after tribocorrosion and aging according to the variant AA-1 for the Inconel 718 alloy

Fig. 10 Scheme for selecting a place of surface analysis after wear tests: 1—wear trace of specimen; 2—magnification area of wear trace, 3—area of EDS chemical analysis
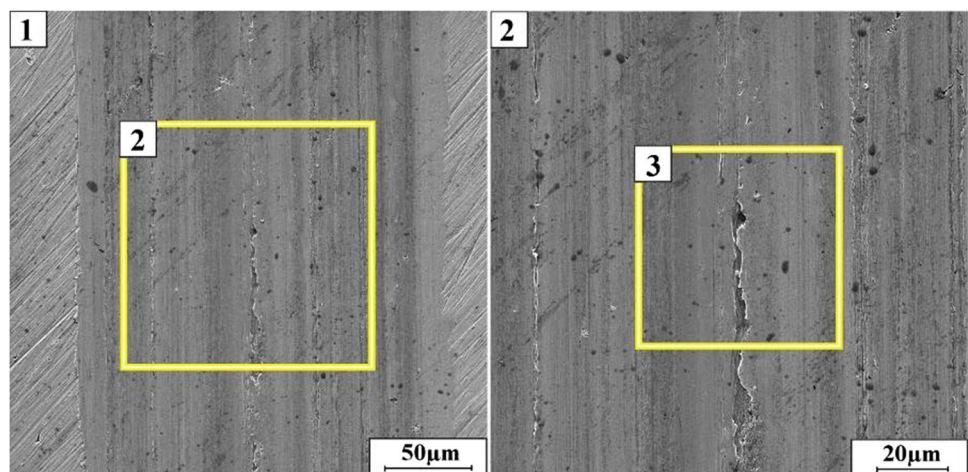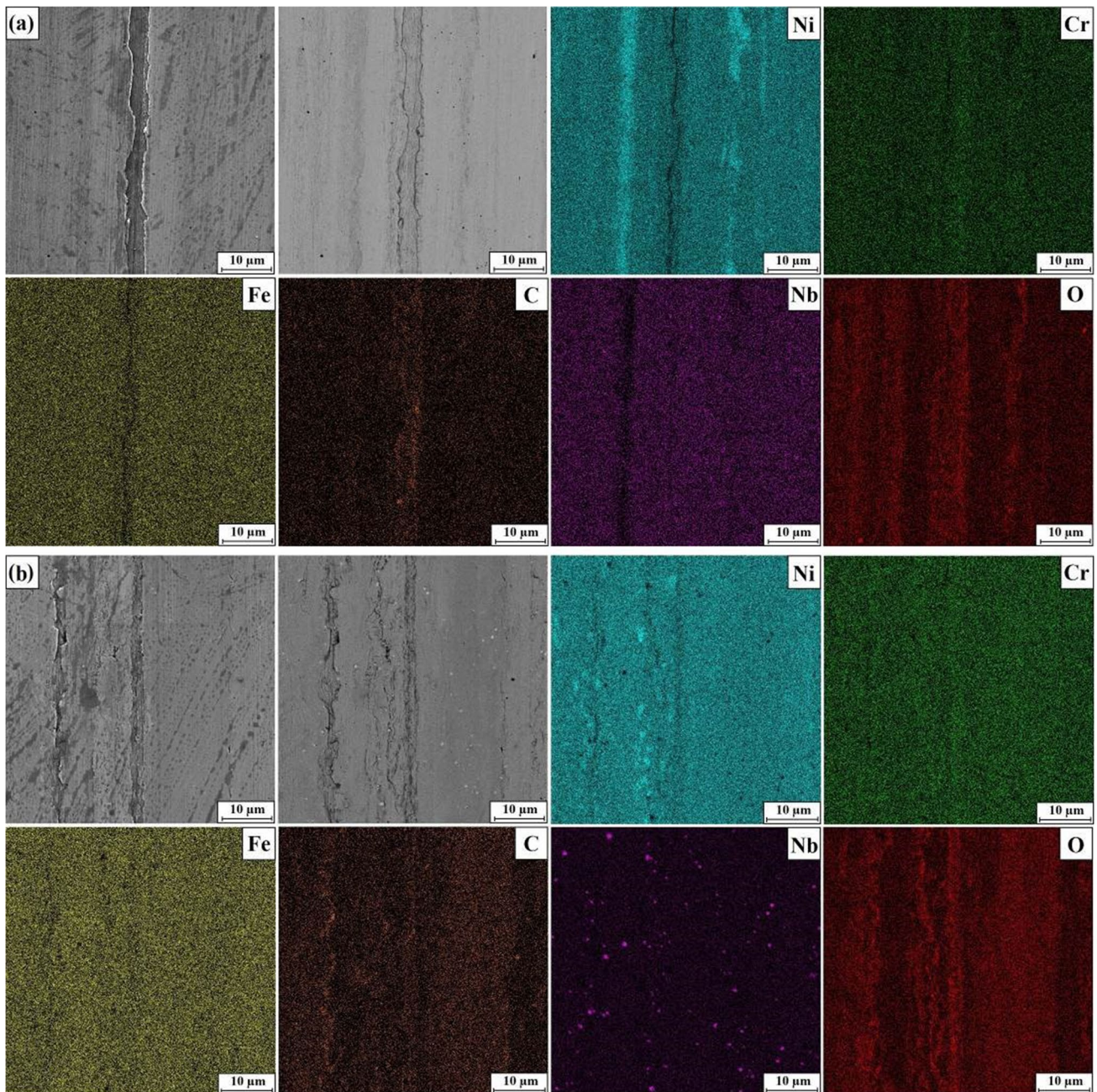
Fig. 11 The wear surface of specimen after mechanical wear test: **a** ROD-1, **b** LPBF-1

produced by the conventional method (Fig. 13a) and additive manufacturing technology (Fig. 13b). In the case of the influence of an additional corrosive agent, which was the NaCl solution, greater changes caused by the wear process were visible. In addition to traces of surface wear in the form of ditches, numerous chippings can also be observed. Chipping marks may become a source of additional defects and may be the result of damage to the friction pair. Notches, surface defects, and oxides can also accelerate crack nucleation.

Figure 14 shows a comparison of the wear surfaces of Inconel 718 specimens produced by the conventional method (Fig. 14a) and the LPBF method (Fig. 14b) subjected to aging at 760 °C/8 h and then tribocorrosion. It can be seen that the effect of the corrosive medium caused greater changes than without this medium (see Fig. 12). The surface condition after mechanical wear of the LPBF-2 specimen is much better than that of the LPBF-1 specimen after the tribocorrosion tests.
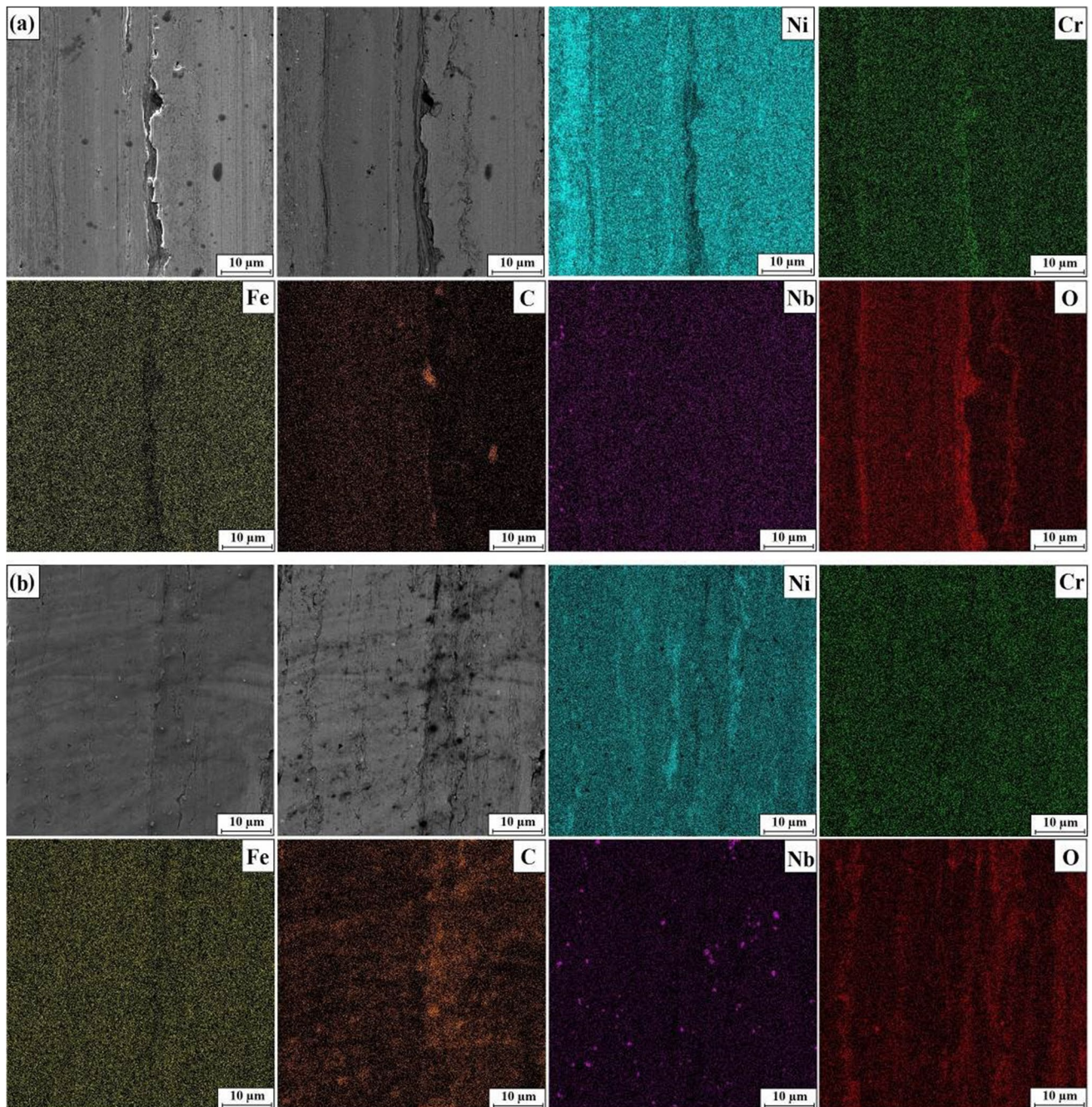
Fig. 12 The wear surface of specimen after mechanical wear test: **a** ROD-2, **b** LPBF-2

In summary, it can be concluded that the clearly visible parallel grooves indicate abrasion as the dominant material removal mechanism. In the case of samples produced conventionally (ROD-1, ROD-2), deeper grooves and chipping are visible in the middle of the wear trace. A deeper groove in the middle of the wear trace may be caused by the abrasive action of the wear particles. In the case of material obtained by the classical technique (ROD), the structure with larger grains can generate larger wear particles. In the middle part

of the wear trace (sphere of contact between the ball and the sample), the greatest unit pressures prevail, which is conducive to more intensive mechanical removal of material (especially in the presence of abrasive). For samples subjected to tribocorrosion, traces of abrasive wear with local material tears are visible (LPBF-1, ROD-2). The mildest forms of tribocorrosive wear were observed for the LPBF-2 material. This material showed the lowest quantitative wear under tribocorrosion conditions (Table 5). Detailed results of point EDS analysis after
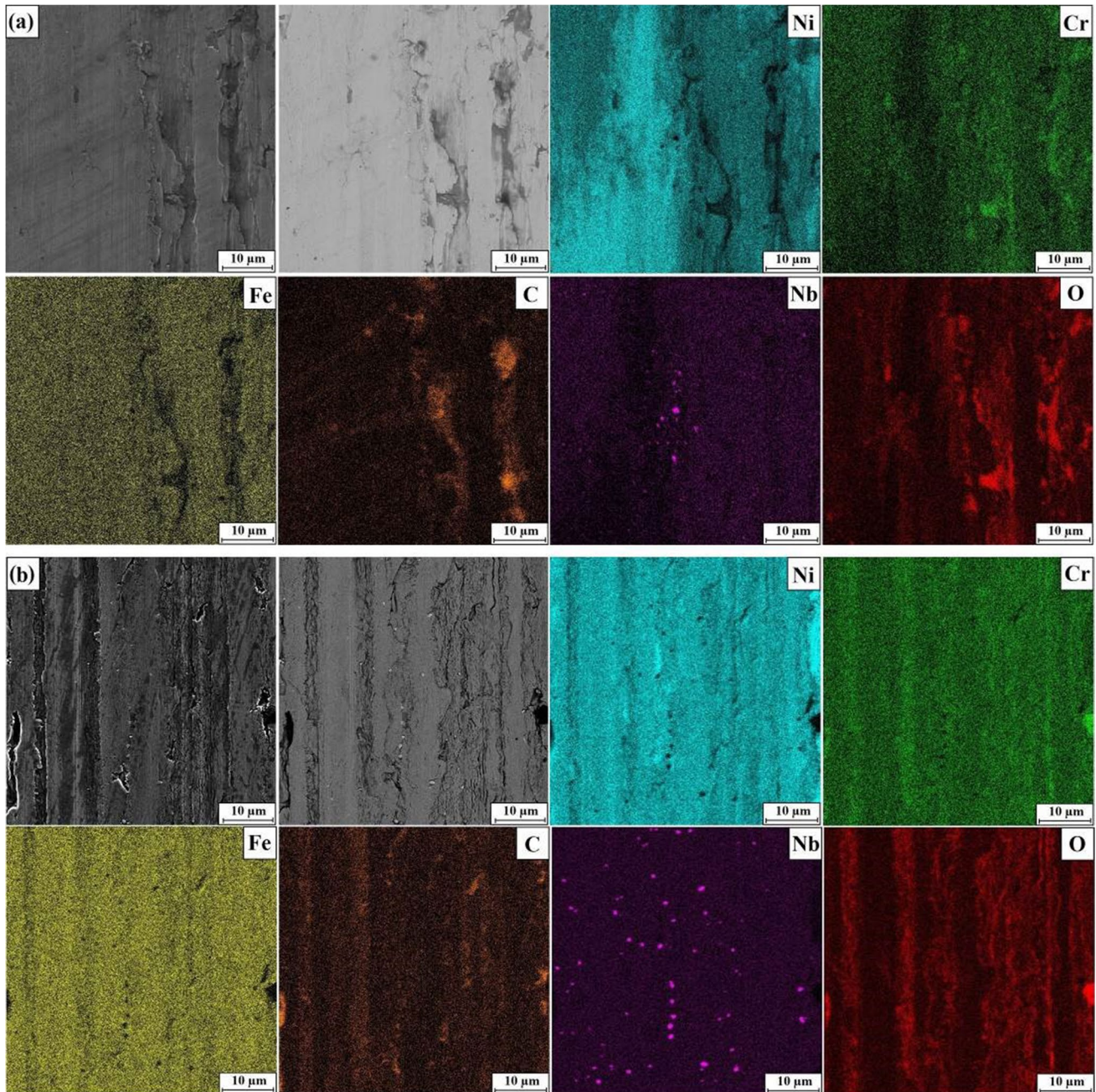
Fig. 13 The wear surface of specimen after tribocorrosion wear test: **a** ROD-1, **b** LPBF-1

tribocorrosion tests are presented in Fig. 15 and in Table 7. It can be noticed that increased oxygen content in the areas of pits and chips was found.

4 Result analysis

The purely mechanical wear (Z_M) of the tested materials is determined by their hardness (Table 4). The highest material loss was found for samples with the lowest hardness (IN718

marked as ROD-2). The dependence of mechanical wear on material hardness is consistent with the Archard model describing the abrasive wear process. Such mechanisms of material removal (micro-scraping) under conditions of frictional-only interactions were observed on the wear traces of all tested IN718 variants (Fig. 12).

Tribocorrosion wear (Z_T) no longer shows such a clear relationship with material hardness. In the case of the AA-1 heat treatment variant, the IN718 material produced by the classic technique (ROD-1) achieves a slightly higher
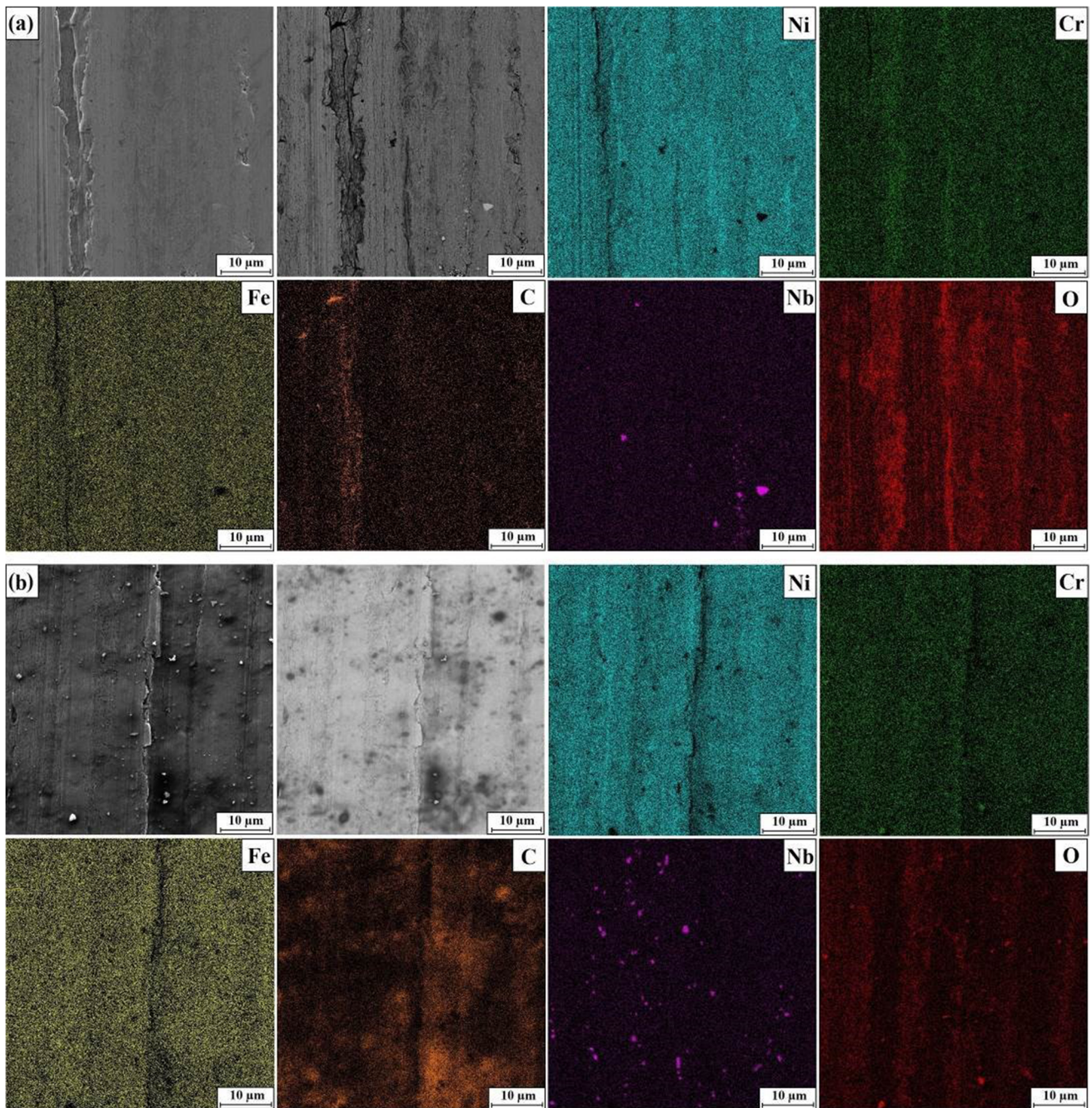
Fig. 14 The wear surface of specimen after tribocorrosion wear test: **a** ROD-2, **b** LPBF-2

hardness (by about 6%) than the printed material (LPBF-1). The IN718 produced by conventional process also exhibits better corrosion resistance in 3.5% NaCl (Table 6). Despite these advantages, a higher material loss under tribocorrosion conditions was found for IN718 marked as ROD-1.

The results presented in Table 6 indicate that tribocorrosion wear is determined by the synergistic effect of friction and corrosion (ΔZ). In the analyzed process, this effect can be associated with the fact that friction has an intensifying effect on the electrochemical processes occurring on the material surface in the contact area between the sample and the counter-sample. Such a mechanism of interactions in the studied frictional association is illustrated by the waveforms of potential changes shown in Fig. 16.

The removal of the passive layer and the electrochemical processes associated with the attempt to partially rebuild it under the conditions of cyclic frictional interactions of the sample and the counter-sample can determine the value

Fig. 15 Areas for chemical composition (EDS) study after tribocorrosion tests: **a** ROD-1, **b** ROD-2, **c** LPBF-1, **d** LPBF-2
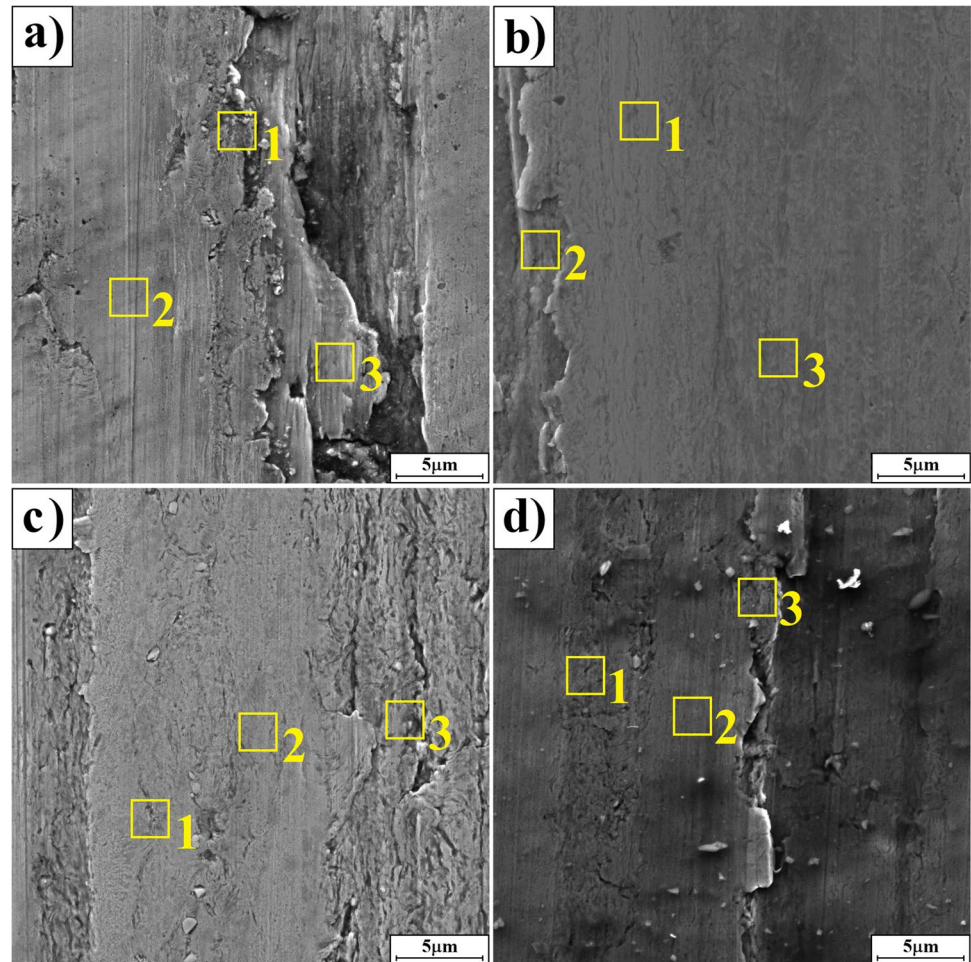

Table 7 Chemical composition (EDS) for areas marked in Fig. 15 [wt.%]

Designation	No	Ni	Fe	Cr	Nb	Mo	Ti	C	O
ROD-1	1	57.2	10.1	10.9	3.4	2.6	0.7	8.2	7.0
	2	53.1	16.0	15.9	4.6	2.8	0.9	4.5	2.2
	3	57.7	14.2	14.0	3.8	2.3	0.8	5.4	1.8
ROD-2	1	50.7	16.3	16.5	4.6	2.9	0.9	4.6	3.5
	2	46.7	13.5	15.3	5.1	2.9	0.8	7.3	8.3
	3	47.0	15.3	16.8	4.8	2.9	0.9	5.6	6.8
LPBF-1	1	51.2	13.8	14.2	3.8	2.5	0.8	9.5	4.2
	2	55.4	13.6	13.1	4.2	2.6	0.7	6.9	3.5
	3	50.2	13.4	13.6	6.7	2.6	0.9	10.2	2.4
LPBF-2	1	46.4	15.1	14.2	9.7	2.5	1.3	10.0	0.9
	2	51.0	14.9	16.0	4.0	2.8	0.7	9.6	1.2
	3	41.8	15.8	16.9	4.2	2.6	0.9	13.0	4.8

of the synergistic effect (ΔZ). The hardness of the material determines the area of the actual contact surface and, consequently, the value of mechanical wear and the area of removal of the passive layer (exposing the surface of the base material). On the other hand, the structure of the material can affect the rate of reconstruction of the passive layer

and the associated wear of the base material due to electrochemical processes.

IN718 produced by the laser powder bed fusion method has a more homogeneous and fine-grained structure (compared to the material produced by the conventional method). In the work of [40, 41], it was found that a large proportion
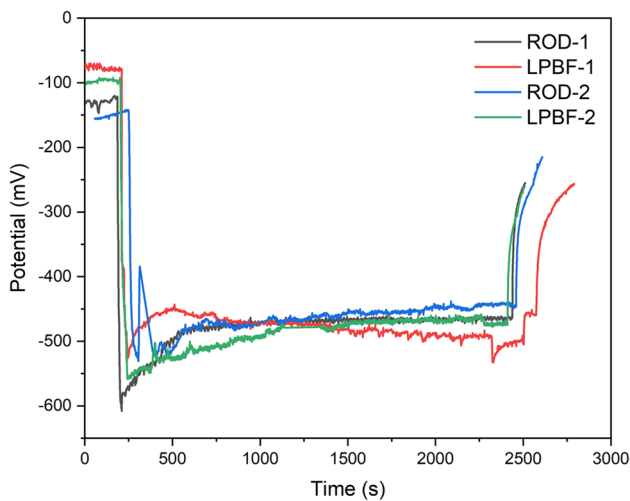
Fig. 16 Potential change during tribocorrosion test

of fine grains in the structure of the material allows better corrosion resistance in a passive environment. Such a mechanism for IN718 obtained by the printing technique was confirmed by the authors in an earlier publication for the non-heat-treated material, LPBF printed material [36].

The passive layer formed on the surface of the LPBF-1 additively manufactured material is more compact (due to the fine-grained structure of the material) and should provide a protective barrier to the corrosive environment sooner. This factor reduces the tribocorrosion wear of the printed material. As a result, the LPBF-1 printed and heat-treated material with lower hardness (with higher mechanical wear and worse corrosion resistance under static conditions) shows better tribocorrosion resistance than the ROD-1 heat-treated variant of the material.

For heat-treated samples of the ROD-2 and LPBF-2 variants, the additively manufactured material has a significantly

higher hardness than the ROD-2 material (by approximately 16%). Consequently, the tribocorrosion wear of the LPBF-2 material is more than 60% less than that of the ROD-2 material. The high hardness results in a smaller actual contact area between the sample and the counter-sample. There is also less surface area for mechanical separation of the substrate material and removal of the passive layer. In addition, the electrochemical processes involved in the restoration of this layer are less intense (due to the fine-grained structure of the printed material).

The results show that among the analyzed variants of the material, the best resistance to tribocorrosion in 3.5% NaCl is provided by IN718 obtained by laser powder bed fusion and heat-treated according to the LPBF-2 variant, including the final step of artificial aging at 760 °C for 8 h, is not the standardized aging procedure, as in ASTM F3055-14a (2021), AMS 2774, and AMS 5662 standards (LPBF-1 was aged according to those standards). This LPBF-2 material combines the advantages of

- manufacturing techniques—laser powder bed fusion method provides a more homogeneous and fine-grained structure after high-temperature heat treatment, which contributes to a more compact passive layer and earlier recovery (with less corrosion of the material) and
- heat treatment—heat treatment in the ROD-2 and LPBF-2 variants provides higher hardness; higher hardness reduces purely mechanical wear (Z_M) and synergistic effect (ΔZ) due to reduced material surface exposed in frictional contact between the sample and counter-sample (smaller area for electrochemical interactions).

In summary, to better illustrate the differences resulting from studies on the tribocorrosion process, the average material loss during the tribocorrosion test for each sample is presented in Fig. 17.

Fig. 17 Average material loss in the tribocorrosion test for all samples
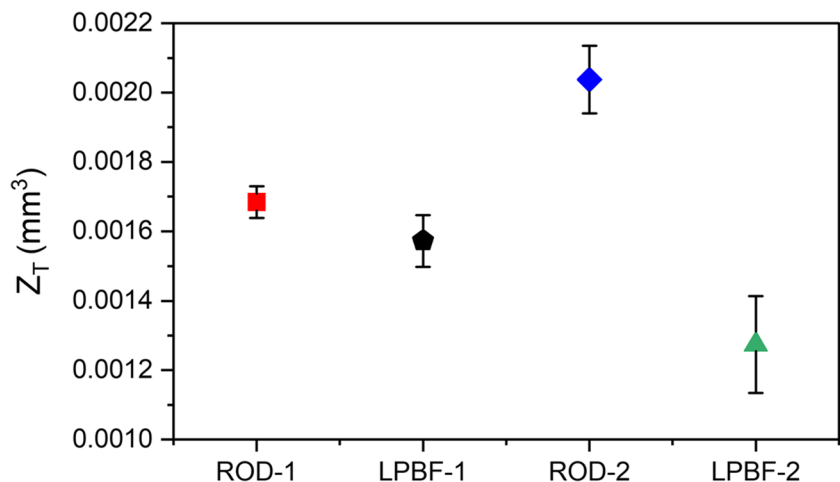
5 Conclusion

Considering the results of the research, the following conclusions can be made:

- The more fine-grained structure of the additive-manufactured IN718 material after heat treatment than that of the cast material results in less wear of the samples when they are exposed to mechanical factors and the corrosive environment—3.5% NaCl.
- Due to the more homogeneous and fine-grained structure of the printed material, the passive layer formed on the surface is more compact and provides a protective barrier for the corrosive environment faster (it reduces material loss caused by electrochemical processes).
- A large number of fine niobium carbides were found on the surface of the additively produced material. Their presence reduces the intensity of abrasive wear.
- During the tests of IN718 samples, there was a synergistic effect between friction and corrosion (ΔZ) which resulted in greater material loss during tribocorrosion wear than during mechanical interaction alone.
- The lowest tribocorrosion wear was achieved for the LPBF-2 sample which indicates heat treatment variant AA-2 for the additively manufactured IN718, especially the one that will be exposed to difficult operating conditions (friction and corrosion at the same time). Heat treatment in the AA-2 variant ensures greater hardness and, consequently, reduced purely mechanical wear (Z_M) and the synergy effect (ΔZ). With increasing hardness, the surface of the material exposed in the frictional contact of the sample and the counter-sample decreases (the area for frictional and electrochemical interactions is smaller).

Data availability All necessary data is shown in the figures and tables within the document. The raw data can be made available upon request.

Declarations

Competing interests The authors declare no competing interests.

References

1. Zhao N, Parthasarathy M, Patil S, Coates D, Myers K, Zhu H, Li W (2023) Direct additive manufacturing of metal parts for automotive applications. J Manuf Syst 68:368–375
2. Li J, Liang D, Chen X, Sun W, Shen X (2024) Applications of 3D printing in tumor treatment. Biomed Technol 5:1–13
3. Sanchez S, Smith P, Xu Z, Gaspard G, Hyde CJ, Wits WW, Ashcroft IA, Chen H, Clare AT (2021) Powder bed fusion of nickel-based superalloys: a review. Int J Mach Tools Manuf 165:10379
4. Nandwana P, Elliott AM, Siddel D, Merriman A, Peter WH, Babu SS (2017) Powder bed binder jet 3D printing of Inconel 718: densification, microstructural evolution and challenges. Curr Opin Solid State Mater Sci 21(4):207–218
5. Felice IO, Shen J, Barragan AFC, Moura IAB, Li B, Wang B, Khodaverdi H, Mohri M, Schell N, Ghafoori E, Santos TG, Oliveira JP (2023) Wire and arc additive manufacturing of Fe-based shape memory alloys: microstructure, mechanical and functional behavior. Mater Design 231:112004
6. Li W, Zhao X, Xu J, Liu H, Cheng Y, Yue Q, Xia W, Gu Y, Zhang Z (2024) Effect of molybdenum on isothermal oxidation behavior of 4th generation nickel-based single crystal superalloys. J Mater Res Technol. 29:1453–1466
7. Seabra M, Azevedo J, Araujo A, Reis L, Pinto E, Alves N, Santos R, Mortagua JP (2016) Selective laser melting (SLM) and topology optimization for lighter aerospace components. Proc Struct Integr 1:289–296
8. Ahmadi M, BozorgniaTabary SAA, Rahmatabadi D, Ebrahimi MS, Abrinia K, Hashemi R (2022) Review of selective laser melting of magnesium alloys: advantages, microstructure and mechanical characterizations, defects, challenges, and applications. J Mater Res Technol 19:1537–1562
9. Suresh S, Sun ChN, Tekumalla S, Rosa V, Mui Ling Nai S, Chung Wen Wong R (2021) Mechanical properties and in vitro cytocompatibility of dense and porous Ti–6Al–4V ELI manufactured by selective laser melting technology for biomedical applications. J Mechan Behav Biomed Mater 123:104712
10. Nandhakumar R, Venkatesan K (2023) A process parameters review on selective laser melting-based additive manufacturing of single and multi-material: microstructure, physical properties, tribological, and surface roughness. Materialstoday Commun 35:105538
11. Yang H, Wang Z, Wang H, Wu Y, Wang H (2023) Microstructure, mechanical property and heat treatment schedule of the

Inconel 718 manufactured by low and high power laser powder bed fusion. Mater Sci Eng A 863:144517

12. Tian X, Wu J, Lu Z, Yang R, Xu L (2022) Effect of powder size segregation on the mechanical properties of hot isostatic pressing Inconel 718 alloys. J Mater Res Technol 21:84–96

13. Zhang Y, Li S, Liu X, Li X, Duan W, Li L, Liu B, Wang G (2023) Additive manufacturing and characterization of microstructure evolution of Inconel 718 superalloy produced by vat photopolymerization. Addit Manuf 61:103367

14. Marques A, Guimaraes B, Bartolomeu F, Miranda FS, Carvalho O (2023) Multi-material Inconel 718 – aluminium parts targeting aerospace applications: a suitable combination of low-weight and thermal properties. Optics Laser Technol 158:108913

15. Holtham N, Davami K (2023) Laser surface treatment of Inconel 617 for next-generation nuclear reactors: a strengthening mechanisms study. Mater Character 202:113024

16. Bhavsar RB, Collins A, Silverman S, (2001) Use of alloy 718 and 725 in oil and gas industry. Conference: Superalloys. TMS (The Alinernls. hletnls S Materials Society)

17. De Bartolomeis A, Newman ST, Jawahir IS, Biermann D, Shokrani A (2021) Future research directions in the machining of Inconel 718. J Mater Process Technol 297:117260

18. Ergene B (2022) Simulation of the production of Inconel 718 and Ti6Al4V biomedical parts with different relative densities by selective laser melting (SLM) method. J Fac Eng Archit Gazi Univ 37(1):469–484

19. Costa TNQ, Dotta TC, Galo R, Soares MEC, Pedrazzi V (2023) Effect of tribocorrosion on surface-treated titanium alloy implants: a systematic review with meta-analysis. J Mech Behav Biomed Mater 145:106008

20. Jablonska M, Jurczak W, Ozimina D, Adamiak M (2023) Increasing operational reliability of a ship by using a composite impeller in the event of hydrophore pump failure. Eksploatacja i Niezawodność/Maintenance Reliability 25:1

21. Cao S, Mischler S (2018) Modeling tribocorrosion of passive metals – a review. Curr Opin Solid State Mater Sci 22(4):127–141

22. Lopez-Ortega A, Arana JL, Bayon R (2018) Tribocorrosion of passive materials: a review on test procedures and standards. Int J Corrosion 2018:1–24

23. Landolt D, Mischler S (2011) Tribocorrosion of passive metals and coatings, ISBN: 978-1-84569-966-6. Woodhead Publishing, Cambridge, UK

24. Landolt D (2006) Electrochemical and materials aspects of tribocorrosion systems. J Phys D Appl Phys 39(15):3121–3127

25. Chen J, Wang J, Yan F, Zhang Q, Li QA (2015) Effect of applied potential on the tribocorrosion behaviors of Monel K500 alloy in artificial seawater. Tribol Int 81:1–8

26. Trembach B, Grin A, Subbotina V, Vynar V, Knyazev S, Zakiev V, Trembach I, Kabatskyi O (2021) Effect of exothermic addition (CuO-Al) on the structure, mechanical properties and abrasive wear resistance of the deposited metal during self-shielded flux-cored arc welding. Tribol Ind 43:452–464

27. Amirjan M, Bozorg M, Sakiani H (2021) Investigation of microstructure and corrosion behavior of IN718 superalloy fabricated by selective laser melting. Mater Chem Phys 263:124368

28. Luo S, Huang W, Yang H, Yang J, Wang Z, Zeng X (2019) Microstructural evolution and corrosion behaviors of Inconel 718 alloy produced by selective laser melting following different heat treatments. Addit Manuf 30:100875

29. Ben Fraj B, Zghal S (2024) Correlation between hardness behavior, shape memory, and superelasticity in Ni-Rich NiTi shape memory alloy. J Mater Eng Perform. https://doi.org/10.1007/s11665-024-09313-w

30. Ben Fraj B, Zghal S, Gahbiche A, Tourki Z (2019) Microstructural effect on the thermomechanical behavior of aged Ni-rich NiTi SMA. Mater Res Express 6(11):1165c7. https://doi.org/10.1088/2053-1591/ab4d78

31. Chen J, Wang J, Chen B, Yan F (2011) Tribocorrosion behaviors of Inconel 625 alloy sliding against 316 steel in seawater. Tribol Trans 54:514–522

32. Stendal J, Fergani O, Yamaguchi H, Espallargas N (2018) A comparative tribocorrosion study of additive manufactured and wrought 316L stainless steel in simulated body fluids. J Bio-Tribo-Corrosion 4(9):1–10

33. Siddaiah A, Kasar A, Kumar P, Akram J, Misra M, Menezes PL (2021) Tribocorrosion behavior of Inconel 718 fabricated by laser powder bed fusion-based additive manufacturing. Coatings 11(2):195

34. Stachowiak A, Zwierzycki W (2012) Analysis of the tribocorrosion mechanisms in a pin-on-plate combination on the example of AISI304 steel. Wear 294–295:277–285

35. Stachowiak A, Wieczorek AN (2021) Comparative tribocorrosion tests of 30CrMo12 cast steel and ADI spheroidal cast iron. Tribol Int 155:106763

36. Stachowiak A, Wieczorek D, Gruber K, Bartkowski D, Bartkowska A, Ulbrich D (2023) Comparison of tribocorrosion resistance of Inconel® 718 alloy manufactured by conventional method and laser powder bed fusion method. Tribol Int 182:108368

37. Zhao Y, Li K, Gargani M, Xiong W (2020) A comparative analysis of Inconel 718 made by additive manufacturing and suction casting: microstructure evolution in homogenization. Add Manuf 36:101404

38. Newell DJ, O'Hara RP, Cobb GR, Palazotto AN, Kirka MM, Burggraf LW, Hess JA (2019) Mitigation of scan strategy effects and material anisotropy through supersolvus annealing in LPBF IN718. Mater Sci Eng A 764:138230

39. Gruber K, Stopyra W, Kobiela K, Madejski B, Malicki M, Kurzynowski T (2022) Mechanical properties of Inconel 718 additively manufactured by laser powder bed fusion after industrial high-temperature heat treatment. J Manuf Process 73:642–659

40. Wang L, Lin Y, Zeng Z, Liu W, Xue Q, Hu L, Zhang J (2007) Electrochemical corrosion behavior of nanocrystalline co coatings explained by higher grain boundary density. Electrochimica Acta 52:4342–4350

41. Gollapudi S (2012) Grain size distribution effects on the corrosion behaviour of materials. Corrosion Sci 62:90–94

42. Silva CC, de Miranda HC, Motta MF, Farias JP, Afonso CRM, Ramirez AJ (2013) New insight on the solidification path of an alloy 625 weld overlay. J Mater Res Technol 2(3):228–237

43. Gruber K, Dziedzic R, Kuźnicka B, Madejski B, Malicki M (2021) Impact of high temperature stress relieving on final properties of Inconel 718 processed by laser powder bed fusion. Mater Sci Eng A 813(141111 Contents):1–15